Predicting Ligand Removal Energetics in Thiolate-protected Nanoclusters from Molecular Complexes

Journal:	*Nanoscale*
Manuscript ID	NR-ART-11-2020-007839.R1
Article Type:	Paper
Date Submitted by the Author:	18-Dec-2020
Complete List of Authors:	Mckay, Julia; University of Pittsburgh, Chemical and Petroleum Engineering Cowan, Michael; University of Pittsburgh, Chemical and Petroleum Engineering Morales-Rivera, Cristian; University of Pittsburgh, Department of Chemical Engineering Mpourmpakis, Giannis; University of Pittsburgh, Chemical and Petroleum Engineering

Predicting Ligand Removal Energetics in Thiolate-protected Nanoclusters from Molecular Complexes

Julia McKay[1], Michael J. Cowan[1], Cristian A. Morales-Rivera[1], and Giannis Mpourmpakis[1,*]

[1]Department of Chemical and Petroleum Engineering, University of Pittsburgh, Pittsburgh, PA 15261, USA

Abstract

Thiolate-protected metal nanoclusters (TPNCs) have attracted great interest in the last few decades due to their high stability, atomically precise structure, and compelling physicochemical properties. Among their various applications, TPNCs exhibit excellent catalytic activity for numerous reactions; however, recent work revealed that these systems must undergo partial ligand removal in order to generate active sites. Despite the importance of ligand removal on both catalysis and stability of TPNCs, the role of ligands and metal type on the process is not well understood. Herein, we utilize Density Functional Theory to understand the energetic interplay between metal-sulfur and sulfur-ligand bond dissociation in metal-thiolate systems. We first probe 66 metal-thiolate molecular complexes across combinations of M = Ag, Au, and Cu with twenty-two different ligands (R). Our results reveal that the energetics to break the metal-sulfur and sulfur-ligand bonds are strongly correlated and can be connected across all complexes through metal atomic ionization potentials. We then extend our work to experimentally relevant $[M_{25}(SR)_{18}]^-$ TPNC, revealing the same correlations at the nanocluster level. Importantly, we unify our work by introducing a simple methodology to predict TPNC ligand removal energetics solely from calculations performed on metal-ligand molecular complexes. Finally, a computational mechanistic study was performed to investigate the hydrogenation pathways for SCH_3-based complexes. The energy barriers for these systems revealed, in addition to thermodynamics, that kinetics favor the break of S-R over the M-S bond in the case of the Au complex. Our computational results rationalize several experimental observations pertinent to ligand effects on TPNCs. Overall, our introduced model provides an accelerated path to predict TPNC ligand removal energies, thus aiding towards targeted design of TPNC catalysts.

*Corresponding author email: gmpourmp@pitt.edu

Introduction

In 1983, Nuzzo and Allara introduced a simple technique to form self-assembled monolayers (SAMs) of organic disulfides on Au substrates[1], paving the way towards a new and exciting field of nanotechnology. Since then, the study of SAMs has exploded due to their versatility in stabilizing and functionalizing metal and metal oxide surfaces[2]. Thiolate ligands on metal surfaces, such as Ag, Au, and Cu, are arguably considered the most-studied SAMs[2-4]. The field further evolved through the Brust-Schiffrin method, a colloidal synthesis technique to create thiolate-stabilized metal nanoparticles[5]. This method, coupled with advancements in size focusing[6] and crystallization techniques[7], led to the discovery of thiolate-protected metal nanoclusters (TPNCs).

TPNCs are ultra-small (tens to a few hundred metal atoms)[8], highly stable, atomically precise structures that exhibit distinct physicochemical properties relative to their larger bulk counterparts[9, 10]. In recent years, TPNCs have motivated substantial research efforts due to their potential for use in many applications, including biological labeling[11], sensing[12], drug delivery[13, 14], optoelectronics[15], and catalysis[16]. In fact, TPNCs have found a broad range of catalytic applications, which extend across thermo-, photo-, and electrocatalysis[17, 18]. Due to the growing number of experimentally determined structures, TPNCs can also act as excellent "nano-models" to fuel computational studies that rationalize their interesting properties[8, 19].

As the name suggests, the metal-ligand (M-S-R) interactions play a crucial role in forming the ordered structure of TPNCs. Thiols have a strong affinity for most metals in the periodic table, especially coinage metals, and these strong interactions deprotonate the thiols to form thiolate ligands[20-21]. The result of these interactions is TPNCs following a single structural rule, known as the divide and protect theory[22]. In short, the theory states that TPNC structures consist of two main components: a highly symmetric metallic core protected by a SAM, or shell, of metal-thiolate staple motifs. Importantly, these interfacial M-S-R bonds are modifiable through metal and ligand selection, which enables control over the morphology, electrochemical properties, and overall functionality of TPNCs[23-26]. However, complete control is still lacking, and there is more work required to elucidate metal-ligand interactions in TPNCs. Continued efforts to understand metal and ligand effects will further expand the potential applications, and thus interest in the field[27-29].

Recent work revealed that TPNCs require partial ligand removal to generate active sites for the electrochemical reduction of CO_2[30]. Austin et al. used computational approaches to show that ligand removal upon $[Au_{25}(SR)_{18}]^-$ is experimentally accessible under electrochemical conditions through two mechanisms: R and SR removal, which generate S and Au active sites on the TPNC, respectively. Furthermore, each active site was found to exhibit different activity and selectivity towards CO_2 reduction[30]. Subsequent work leveraged the thermodynamic stability model[31] to

show that the Au_{25} TPNC maintains stability after both mechanisms of partial ligand removal, supporting experimental results of its robust catalytic performance[32]. Due to the nature of the ligand removal mechanisms, both the M-S and S-R bond energetics play critical roles in activating TPNC catalysts. Moreover, understanding the interplay between these adjacent bonds can aid in catalyst design by enhancing selectivity through controlled S or M active site generation.

Despite the crucial role of metal-ligand interactions for TPNCs, the electronic effects of ligand and metal type in M-S-R bonds is not fully realized. Understanding these effects, and how they influence the ligand removal process, could provide an opportunity to better design TPNCs for targeted applications in catalysis. Thus, the work herein applies Density Functional Theory (DFT) to answer how metal and ligand type affect M-S-R bond energetics, especially towards TPNC ligand removal. We first perform DFT calculations to probe M-S and S-R bond energetics in metal-thiolate molecular complexes across combinations of Ag, Au, and Cu with twenty-two different ligands, revealing correlated properties between these adjacent bonds. We then extend our analysis to investigate ligand removal energetics on TPNCs and relate the metal-ligand-bond energetics between the molecular complex and nanoclusters. Importantly, we introduce a simple methodology to predict TPNC ligand removal energetics from calculations performed solely on metal-ligand molecular complexes.
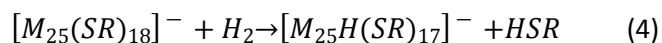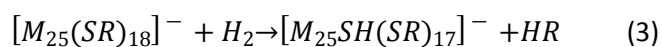
Computational Details

DFT calculations were performed to simulate the thermodynamics of metal-ligand hydrogenation reactions (Equations 1 and 2), consisting of combinations of twenty-two ligands and three metals (Ag, Au, Cu), using Gaussian 09 [33]. The Becke's three parameter hybrid functional incorporating the correlation functional of Lee, Yang, and Parr (B3LYP) [34, 35] was used along with the LANL2DZ (Los Alamos National Laboratory 2 double ζ) basis set[36]. Each molecular system was relaxed without any symmetry constraints with self-consistent field (SCF) convergence to 10^{-6} Ha. All calculations were performed at neutral charge state and singlet multiplicity. Vibrational analysis was further performed on the optimized molecules to determine that total minima were obtained (absence if imaginary frequencies) and to calculate free energies at 298.15 K through statistical thermodynamics, as implemented in Gaussian. Gibbs Free energies were calculated for two ligand removal modes: "break S-R" (Equation 1) and "break M-S" (Equation 2).

$$MSR + H_2 \rightarrow RH + MSH \qquad (1)$$
$$MSR + H_2 \rightarrow HSR + MH \qquad (2)$$

Natural bond orbital (NBO)[37, 38] calculations were performed, as implemented in Gaussian 09 (NBO version 3.1)[33], to determine the Wiberg bond indices[39], *i.e.* bond orders, between M and the closest N in AuMBI, AuTG, AgMBI, AgTG, CuMBI and CuTG.
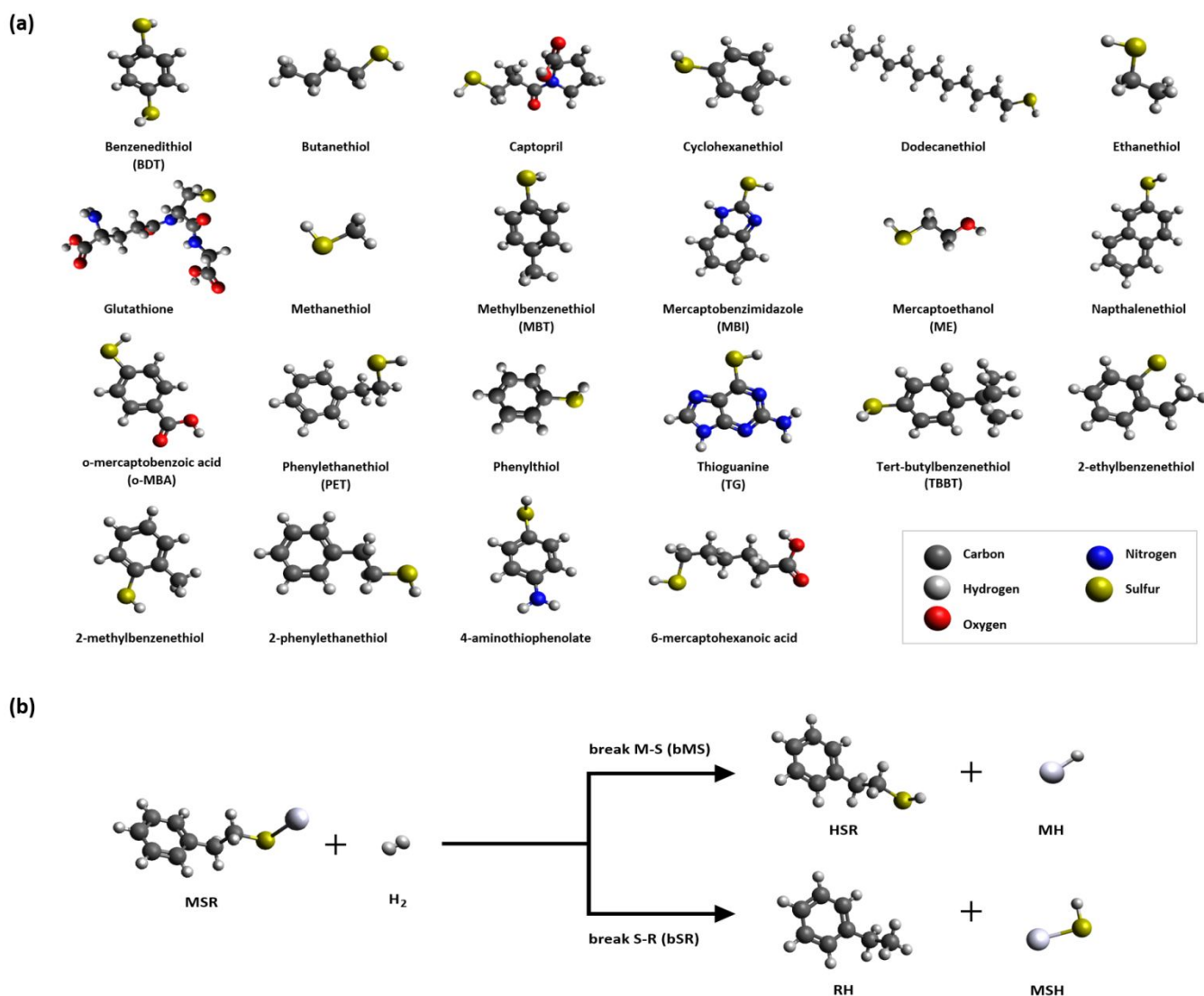
To simulate the $[M_{25}(SR)_{18}]^-$ TPNC, where M = Ag, Au, or Cu and SR = PET or SCH_3, we used the CP2K package version 6.1[40, 41]. TPNCs were constructed from the experimental structure of $[Au_{25}(PET)_{18}]^-$, which was taken from literature,[42] using Avogadro to replace metals and ligands[43]. In addition to PET ligands, methylthiolates were also considered due to their low steric hindrance (to avoid local minima during geometry optimization) and previous success as a viable substitution to capture TPNC electronic properties with DFT[30, 32]. All calculations were performed using the Perdew-Burke-Ernzerhof (PBE) exchange-correlation functional[44] along with the double-ζ valence polarized (DZVP) basis set[45] and the Goedecker, Teter, and Hutter (GTH) short range pseudopotentials[46]. The nanoclusters were centered in a cubic box with a box side length of 37 Å. The system was then relaxed until the max interatomic force threshold was 0.023 eV/Å. Iterative calculations utilizing the SCF method were used until the system energy converged to 10^{-7} Ha. All calculations on the $M_{25}(SR)_{18}$ TPNCs were performed with a charge state of -1 since the original $Au_{25}(SR)_{18}$ is most stable in its anionic form (i.e. as a highly stable superatom).[47, 48] Fully-protected and partially-protected TPNCs were run with singlet multiplicity. In addition, Fermi–Dirac smearing was used with an electronic temperature of 300 K, as implemented in CP2K. Ligand removal energies were calculated for two removal modes: remove R (Equation 3) and remove SR (Equation 4), which act as analogues to "break S-R" and "break M-S" metal-ligand reactions, respectively.

$$[M_{25}(SR)_{18}]^- + H_2 \rightarrow [M_{25}SH(SR)_{17}]^- + HR \qquad (3)$$

$$[M_{25}(SR)_{18}]^- + H_2 \rightarrow [M_{25}H(SR)_{17}]^- + HSR \qquad (4)$$

Results & Discussion

We first performed structure optimizations on sixty-six different metal-thiolate complexes. The M-S-R complexes consisted of M = Ag, Au, or Cu bonded to one of twenty-two different thiol ligands as shown in Figure 1a. We selected a broad range of systems in order to investigate the structural and electronic effects of both ligand and metal type on M-S-R bond energetics. Importantly, the M-S-R complexes selected enable systematic comparisons to probe metal and ligand effects independently. Additionally, we included many common ligands used in TPNC synthesis (glutathione[49], PET[50], TBBT[51], o-MBA[52], MBT[50], and cyclohexanethiol[49]) to ensure that the results are applicable to TPNC research. To study the bond energetics in the M-S-R complexes, we examined two hydrogenation reaction schemes (Figure 1b):

breaking the S-R bond (Equation 1) to produce RH and MSH, and breaking the M-S bond (Equation 2) to produce HSR and MH, which are relevant to hydrogenation and reduction reactions[30, 32, 53-56]. Break S-R and break M-S are equivalent to removing the R group and the SR group from the complex, respectively. We note that previous work has studied hydrogen-based ligand removal to generate catalytically active sites on TPNCs[30, 32, 56]. The studies found that the break S-R and break M-S are thermodynamically downhill under electrochemically reducing conditions (i.e. applied voltage) with the break S-R being more favorable.

(a)

| Benzenedithiol (BDT) | Butanethiol | Captopril | Cyclohexanethiol | Dodecanethiol | Ethanethiol |

| Glutathione | Methanethiol | Methylbenzenethiol (MBT) | Mercaptobenzimidazole (MBI) | Mercaptoethanol (ME) | Napthalenethiol |

| o-mercaptobenzoic acid (o-MBA) | Phenylethanethiol (PET) | Phenylthiol | Thioguanine (TG) | Tert-butylbenzenethiol (TBBT) | 2-ethylbenzenethiol |

| 2-methylbenzenethiol | 2-phenylethanethiol | 4-aminothiophenolate | 6-mercaptohexanoic acid |

Carbon   Nitrogen
Hydrogen   Sulfur
Oxygen

(b)

break M-S (bMS)

MSR + H₂ →

HSR + MH

break S-R (bSR)

RH + MSH

Figure 1. (a) Fully optimized metal-thiol complexes. Yellow balls represent sulfur atoms. Grey and white correspond to carbon and hydrogen atoms, respectively. Blue and red balls represent nitrogen and oxygen, respectively. **(b)** Schematic of break S-R and break M-S reactions at the metal-ligand complex level. The AgPET complex is shown as an example. The reaction thermodynamics were studied for 66 molecular complexes made from combinations of Au, Ag, and Cu with twenty-two different ligands.

Gibbs free energies of reaction were calculated for the break S-R (Equation 5) and break M-S (Equation 6). The results were plotted as ΔG^{bSR} vs. ΔG^{bMS} in Figure 2.

$$\Delta G^{bSR} = [G_{RH} + G_{MSH}] - [G_{MSR} + G_{H_2}] \qquad (5)$$

$$\Delta G^{bMS} = [G_{HSR} + G_{MH}] - [G_{MSR} + G_{H_2}] \qquad (6)$$
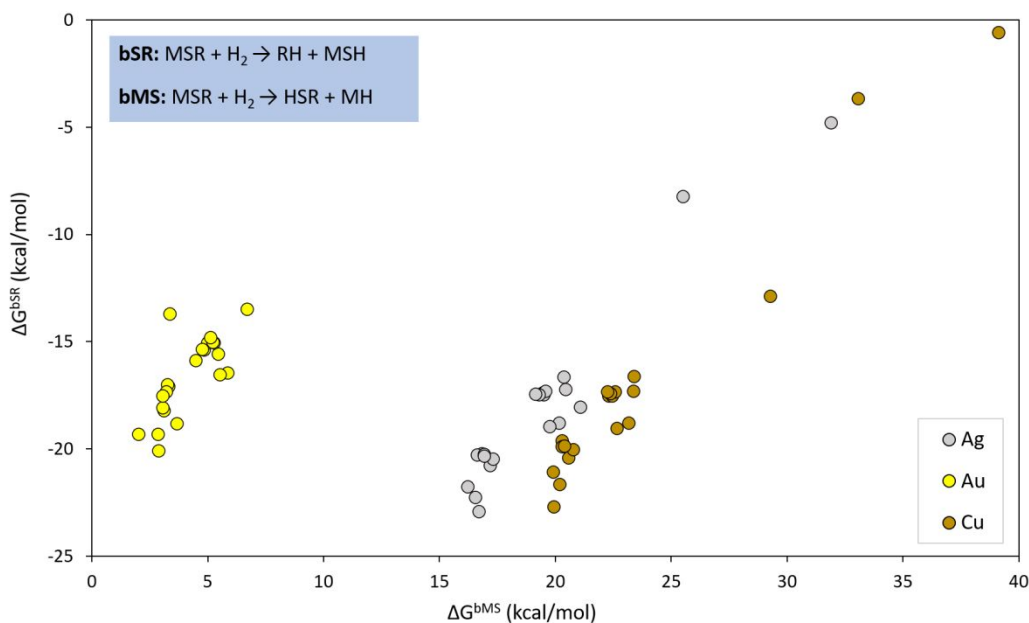
Figure 2. Comparing Gibbs Free Energy of break M-S and break S-R reactions. Each point represents a different molecular complex and is colored based on metal type (Ag, Au, Cu).

As shown in Figure 2, for all ligand types and metals, the break S-R reaction is more thermodynamically favorable than break M-S. In fact, all ΔG^{bSR} are found to be negative (spontaneous) while all ΔG^{bMS} are positive. The results suggest that the M-S bond is much stronger compared the S-R bond for these metal-thiolate complexes. When comparing the impact of the metal types on the bond energetics, one can observe that Au clearly exhibits different behavior than Ag and Cu. For example, it is interesting to note from Figure 2 that Au is the least sensitive to ligand type, compared to Cu and Ag, which exhibit a wide range of energetics. Upon further inspection of the results (bar graphs in Figures S1 and S2), we find that ligands containing a nitrogen bonded to an alpha carbon (MBI and TG) or beta carbon (glutathione) are the ones causing the deviation for Ag and Cu systems (data points on the upper right part of Figure 2). To understand why these specific ligands invoke a stronger effect from Ag and Cu, we need to analyze the results across single ligand

types. To do this, we solved linear regression lines $\left(i.e. \ \Delta G^{bMS} = m\Delta G^{bSR} + b \right)$ between points with the same ligand type (three data points corresponding to different metal atoms). Figure S3 plots the slopes (m) solved as a bar graph. Immediately, one can observe that in every case except for glutathione, MBI, and TG, the slope is negative, which means as one reaction (either bMS or bSR) becomes more thermodynamically favorable, the other one becomes less favorable. In other words, a negative slope indicates an inverse relationship between M-S and S-R bond strengths, which is the expected result based on general chemistry[57]. Charge is transferred between adjacent bonds and as one bond is strengthened, the other one should be weakened due to the displacement of electrons between the bonds. In stark contrast, glutathione, MBI, and TG complexes exhibit positive slopes, which means that both M-S and S-R bonds are strengthened or weakened together. This can be rationalized through a charge and structure analysis of the initial metal-thiolate complexes. Figure S4 shows the structure and Mulliken charge distributions for the Au, Ag, and Cu complexes with TG and MBI ligands. Focusing on the metals, we observe that Ag and Cu donate charge whereas Au does not. Furthermore, Figure S4 reveals that Ag and Cu appear to coordinate with a N in each ligand, and the nitrogens in these cases are found to localize more charge relative to the Au systems. As a result, the Ag and Cu metal atoms exhibit enhanced (electrostatic) interactions with the N of the ligands, thus stabilizing the entire complex and causing an increase to both ΔG^{bMS} and ΔG^{bSR}. The coordination can be described quantitatively as well through Figure S5, which depicts Metal-Sulfur-Carbon (M-S-C) bond angle vs. Metal-Nitrogen (M-N) distance for these structures. Figure S5 shows that metal-thiolate complexes containing Au have the largest M-N distance as well as the largest M-S-C bond angle. Cu has the shortest distance and smallest angle with Ag close behind. The results suggest that Au-S bonds lack flexibility compared to Ag-S and Cu-S bonds, which is in agreement with previous work comparing Au-S and Ag-S binding properties in TPNCs.[58] Of note, the Ag-N and Cu-N distances are within the experimentally observed range of bonding[59-61]. Therefore, to gain further insight into these interactions, we computed the bond orders of the metal-nitrogen pairs in the MBI and TG complexes (Table S1). Our results reveal that for both ligand types, Au-N exhibit virtually no bonding (bond order ~0.06). In contrast, Ag-N and Cu-N pairs exhibit relatively larger bond orders of ~0.17 and ~0.23, respectively, which suggests some bonding interactions between these metal-nitrogen pairs still dominate though electrostatics. Nevertheless, the bond analysis provides further evidence for the differences in bond energetics observed for Au complexes compared to Ag and Cu systems. Taken together, the analysis rationalizes the lack of ligand sensitivity within Au-based complexes.

The differences in bond energetics between metal types can be explained by the atomic ionization potential (IP) of the metals. We confirmed this by leveraging experimental metal IPs from literature[62] to bridge ΔG^{bSR} and ΔG^{bMS}

through multivariate linear regression, as shown in Figure 3.
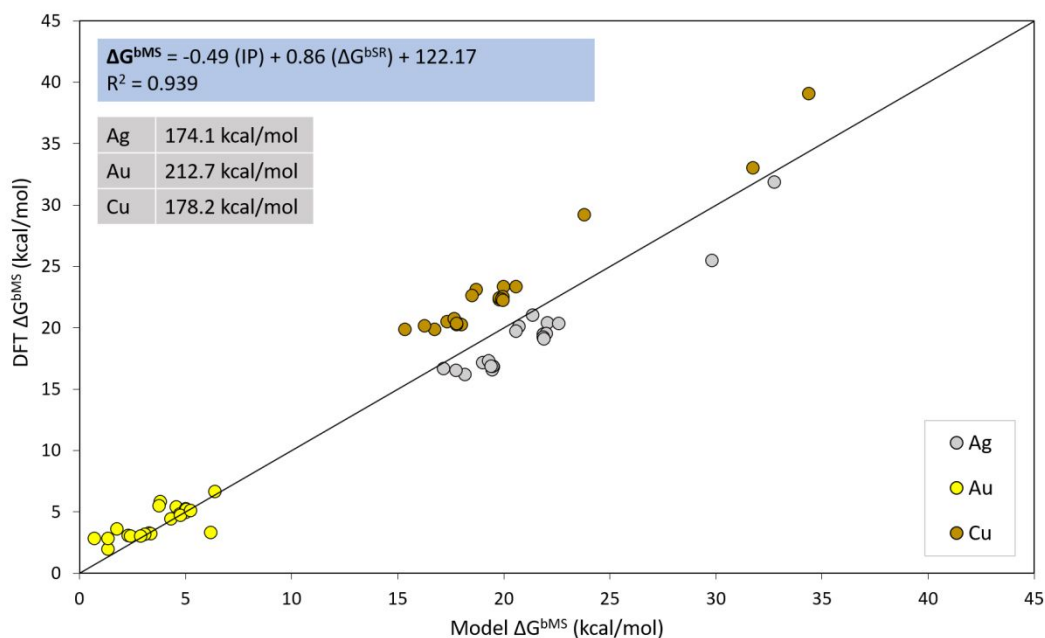
Figure 3. Linear regression model (x-axis Model ΔG^{bMS}, equation in blue box) presented as a parity plot, which connects the break S-R and break M-S reaction free energies through metal IPs[62] (shown in red). Points are colored based on metal type. Perfect parity is represented as a solid black line.

The parity plot in Figure 3 compares the DFT free energy of the break M-S reaction on the y-axis to the predicted values from the model on the x-axis (linear model in blue box of Figure 3). The results reveal that the break S-R and break M-S reactions can be connected across all complexes by incorporating metal IP. IP is the energy required to remove an electron from an atom, (in this case, one of the three metal types), and is thus a metric of charge transfer. Since Au has the largest IP, it requires the most energy to remove an electron or to donate charge. Break M-S is easiest for Au across all of the ligands because Au is not donating charge, which makes the M-S bond weaker compared to Ag- and Cu-based complexes. Furthermore, ΔG^{bMS} for Au is less sensitive to ligand type, which could explain why certain Au-based TPNCs can be synthesized with various different ligands[63-65]. Metal charge transfer leads to stronger M-S bonds, which is revealed in Figure 3 by larger ΔG^{bMS} for Ag and Cu systems. Moreover, lower IP makes Ag and Cu more sensitive to ligand type, causing a wider spread of reaction free energies compared to Au complexes. The increased sensitivity leads to stronger charge transfer invoked by certain ligands, which in turn leads to further enhanced stability compared to other metal thiolate complexes.

8

We next extended our calculations to the nanocluster level to investigate if there is a relationship between metal-ligand-bond energetics in M-S-R complexes and metal TPNCs. As previously mentioned, ligand removal is crucial to generating active sites on TPNC catalysts[30, 32]. Therefore, the effects of ligand removal were examined for several TPNCs. The energy required to remove a single ligand from a TPNC, referred to as ligand removal energy (LRE), reveals information about the stability of the system as well as the local M-S-R bond energetics. Collecting information about the LRE for each of the TPNCs studied in this work is a valuable tool because it allows for connections to be made between metal-thiolate molecular complex and TPNC calculations. All TPNC ligand removal calculations were performed on the well-known $[M_{25}(SR)_{18}]^-$, which is arguably the most studied system within this materials class[65]. Six monometallic TPNCs were studied, consisting of M = Au, Ag, and Cu and SR = PET and SCH_3. PET was chosen due to experimental relevance as the $[M_{25}(SR)_{18}]^-$ structure was first experimentally determined with PET ligands[42, 66]. In addition, we selected methylthiolate (SCH_3) as a second example ligand to avoid steric hindrance concerns, which in turn avoids our geometry optimizations from converging on local minima. The $[M_{25}(SR)_{18}]^-$ TPNC, following the divide and protect theory[22], consists of a thirteen-metal-atom icosahedron core (Figure 4a) protected by a shell of six dimer staple motifs (Figure 4b). Due to the high symmetry of the structure (D_{2h} excluding R groups[9]), there are two unique ligand removal sites, labeled A and B in Figure 4c. The combination of the metallic core and the six staple motifs form the full TPNC (Figure 4d).

We note that the unique sites labeled in Figure 4c distinguish between different metal-sulfur coordination environments. The sulfur at site A is bonded to a core M(0) and a shell M(I) atom while the site B sulfur is bonded to two shell M(I) atoms. Previous experimental work found that these binding modes dictate thermal stability of the ligand sites[67], suggesting that the sites could exhibit different ligand removal energetics. Due to the dynamic nature of the thiolate ligands in nanoclusters[68], we assume negligible steric effects on ligand removal relative to the effects of sulfur binding modes. Thus, the $[M_{25}(SR)_{18}]^-$ provides an ideal two-site system to conduct our systematic ligand removal study.
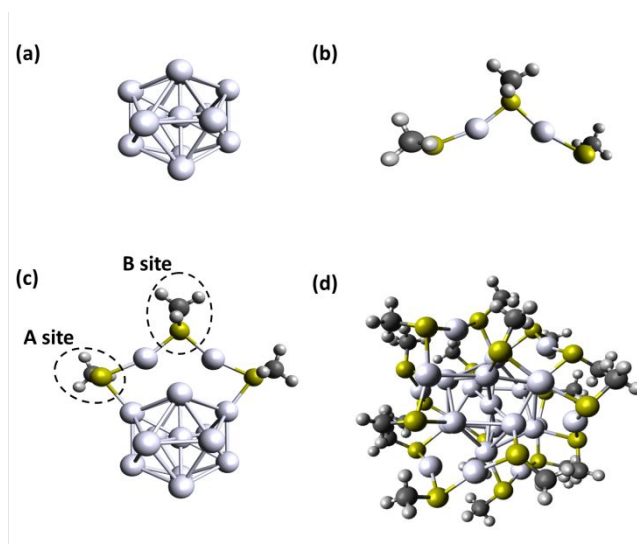
Figure 4. Structural components of the $[Ag_{25}(SCH_3)_{18}]^-$ TPNC: **(a)** highly symmetric metallic core, **(b)** dimer staple motif, **(c)** single staple motif attached to core to highlight the two symmetrically unique ligand removal sites (A and B) and **(d)** full nanocluster.
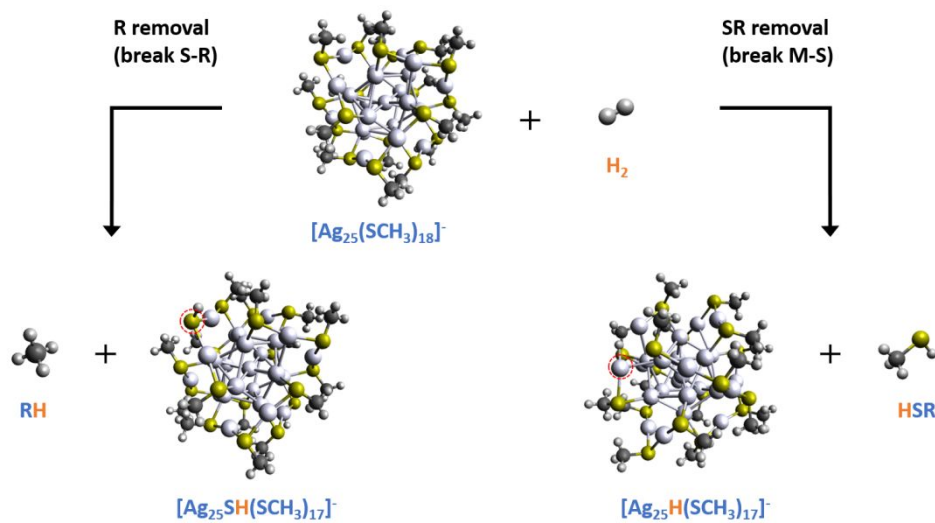

Figure 5. Ligand removal modes through hydrogenation reactions, which are analogous to metal-ligand complex reactions. R removal (break S-R, left) leaves the sulfur exposed and produces RH, while SR removal (break M-S, right) leaves the metal exposed and produces HSR. Hydrogen atoms bond to the active sites in the ligand-removed products (circled in red).

Figure 5 shows the ligand removal modes on the TPNCs. TPNCs undergo two types of ligand removal: R removal and SR removal. We investigated LREs for hydrogenation reactions that are analogous to the previous metal-ligand complex reactions. Once again, we examined the break S-R (Figure 5 left, which corresponds to R removal) and break M-S (Figure 5 right, which corresponds to SR removal). LREs for break S-R and break M-S are calculated using Eqns. 7 and 8, respectively. We note that although our TPNC calculations do not incorporate vibrational contributions (due to increased computational cost), results in literature suggest that we can expect similar trends between LRE and free energy of reaction for these systems[16]. LRE calculations were conducted for the two reactions with six monometallic TPNCs (three metals, two ligand types) and on A and B removal sites.

$$\text{LRE}^{\text{bSR}} = \left[E_{[M_{25}SH(SR)_{17}]^-} + E_{HR}\right] - \left[E_{[M_{25}(SR)_{18}]^-} + E_{H_2}\right] \qquad (7)$$

$$\text{LRE}^{\text{bMS}} = \left[E_{[M_{25}H(SR)_{17}]^-} + E_{HSR}\right] - \left[E_{[M_{25}(SR)_{18}]^-} + E_{H_2}\right] \qquad (8)$$
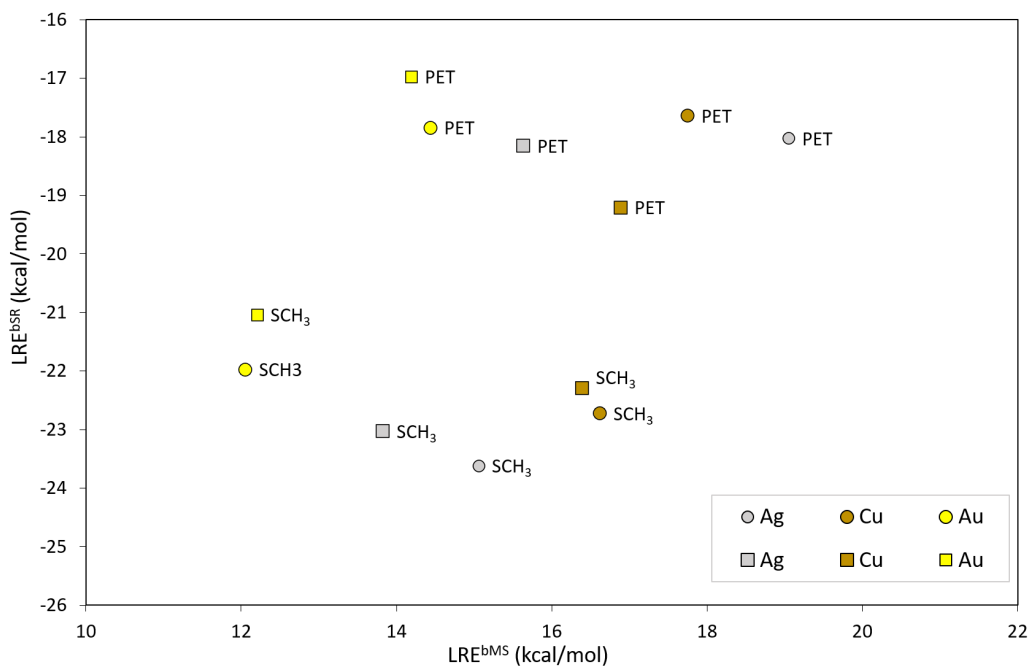
Figure 6. Comparing LRE$^{\text{bMS}}$ and LRE$^{\text{bSR}}$ for TPNCs. Shapes indicate the A (circles) and B (squares) removal sites on the [M$_{25}$(SR)$_{18}$]$^-$. The points are colored according to the three metal types (Ag, Au, Cu) and the ligand types are labeled (SCH$_3$ and PET).

All LRE results are plotted in Figure 6, which reveals that the same trends are observed in break M-S vs. break S-R when compared to complex-level reactions. Once again, the M-S bond is stronger than the S-R bond and therefore breaking the S-R bond is more favorable. This means that ligand removal involving the removal of only the R group is easier than removing the SR group, which aligns with previous observations[8]. This is true regardless of the metal or ligand type that was examined. Unlike the metal-ligand complexes, the TPNCs provide two symmetrically unique local environments to probe ligand removal energetics (Figure 4c). Based on Figure 6, there are significant, non-systematic differences in LREs between the A (circles) and B (squares) sites. The changes are most pronounced for PET ligands on Ag and Cu TPNCs where we see LRE^{bSR} (y axis, Figure 6) become more favorable for B sites, which is the opposite trend compared to the SCH_3 results. Of note, Au does not exhibit the same switch in trend between ligands. Instead A site LRE^{bSR} is more favorable than B site removal for $[Au_{25}(SCH_3)_{18}]^-$ and $[Au_{25}(PET)_{18}]^-$. We hypothesize that the change in trend is due to the lower IP of Ag and Cu relative to Au. For the B site (Figure 4c), lower IP enables the two shell M(I) atoms (i.e. Ag or Cu) to donate more charge to the S site in the break S-R product, stabilizing the TPNC for a more favorable LRE^{bSR}. The hypothesis is supported by our M-S-R calculations where we found that the Au-S bond is not as sensitive to ligand type due to a higher IP. Nevertheless, these variations suggest that results from each removal site should be examined separately. By doing so, we generate linear regression models for each site in Figure S6 to connect LRE^{bMS} with LRE^{bSR} and metal IP. The results reveal that the site-specific LRE data follows the same trends as the break M-S and break S-R relationships discovered for M-S-R complexes (Figure 3). However, we note that results on the B site (Figure S6b) do not trend as strongly as the A site results ($R^2 = 0.651$ vs. $R^2 = 0.942$, respectively). Upon further analysis, we find that the H saturation in the break M-S products exhibit different configurations between A and B sites. Notably, the H in the B site products (red squares in Figure S7a) coordinate equally with the two shell metal active sites (Figure S7c). This is in contrast to the A site products, which show stronger coordination to a single shell metal atom (Figure S7b), similar to H-S coordination in the break S-R reaction products. Thus, the B site products from break M-S reactions on TPNCs are different than all other reactions studied (including the metal-ligand complex reactions), which explains the weaker trends observed in Figure S6b. Nevertheless, the results reveal that there are similar electronic effects governing ligand removal energetics between M-S-R complexes and TPNCs.
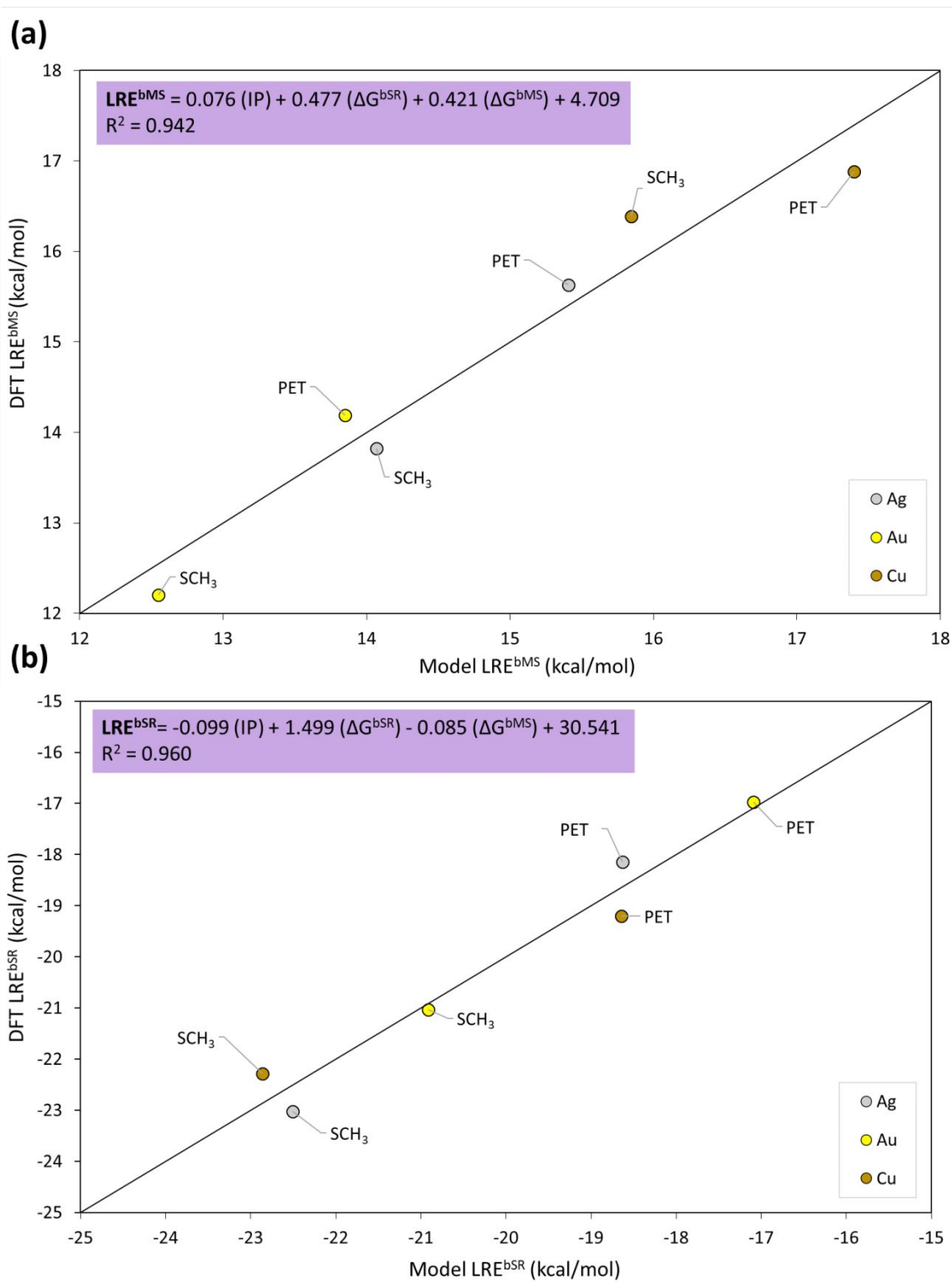
Figure 7. Parity plots of linear regression models (x-axis Model LRE^{bSR} and equations in purple boxes) that display strong correlations between ΔG^{bSR}, ΔG^{bMS}, and metal IP with B removal site LREs for the **(a)** break M-S and **(b)** break S-R TPNC reactions. Perfect parity is represented as a solid black line.

To further exploit these realized trends, we leverage all of our calculations to produce linear regression models that predict nanocluster LREs solely from metal-ligand molecular complex reaction energetics (ΔG_{bMS}, ΔG_{bSR}) and metal IP. Parity plots shown in Figure 7 were generated based on the B site of LRE calculations. Separate plots were made for break M-S (Figure 7a) and break S-R (Figure 7b). The values generated in the models are shown on the x-axis and the DFT calculated values are shown on the y-axis. The results in Figure 7 show that metal-ligand molecular complex reaction energetics (ΔG_{bMS}, ΔG_{bSR}) and metal IPs can be used to capture TPNC LREs. In fact, both models based on ligand removal from a B site exhibit high accuracy, with $R^2 > 0.94$. We note that similar accuracies ($R^2 > 0.92$) are found for A site LREs, as shown in Figure S8 of the Supporting Information. With the use of these models, we can predict ligand removal energetics on full nanoclusters for multiple ligand and metal types by simply understanding the M-S-R complex energetics. Therefore, the generated models provide a screening tool to down-select ligand candidates for targeted ligand removal energetics and to rationalize interfacial bond strengths in TPNCs, relevant to their overall stability. Furthermore, since full TPNC calculations are not required, this means that this method saves computational cost. With ligand removal being of paramount importance to generating catalytic active sites on TPNCs[30, 32, 56], these models open new avenues toward accelerated TPNC catalyst design (e.g. selective exposure of surface S atoms as active sites).

Our work herein focuses on the thermodynamics of break M-S and break S-R reactions. However, it is important to understand the kinetics that govern these competing reactions. Therefore, we employed DFT calculations and the energy span model[68] to determine transition states and turnover frequencies (TOF), respectively, of break M-S and break S-R reactions on select metal-thiolate complexes ($MSCH_3$, M = Au, Ag, Cu). The detailed methods and analysis of our mechanistic study are presented in the SI file. The first-principles-based TOF calculations reveal metal-dependent reaction preference based on kinetics. $AuSCH_3$ kinetically prefers break S-R (Figure S9), which matches the thermodynamic preference, while $AgSCH_3$ and $CuSCH_3$ instead prefer break M-S (Figures S10 and S11). The break S-R kinetic preference for Au supports previous work that shows high catalytic performance of Au TPNCs due to the break S-R reaction creating active S sites[30, 32, 56]. We note that our TOF calculations are performed at room temperature to serve as a comparative, quantitative metric for the kinetic preference between reactions. A more thorough understanding of the kinetics of ligand dissociation on TPNCs that account for catalytic conditions (e.g. under applied potential[56] and/or at elevated temperatures), will be a potential future effort.

Conclusions

In this work, we examined M-S-R bond energetics in metal-thiolate complexes and TPNCs to answer two key questions: i) How do metals and ligands affect M-S-R bond energetics, and ii) Is there any relationship between metal-thiolate bond energetics in molecular complexes and TPNCs? Gibbs Free Energy of break S-R and break M-S reactions for 66 different metal-thiolate complexes revealed that breaking the M-S bond is thermodynamically more difficult, and therefore the M-S bond is stronger than the S-R bond. Additionally, Au was determined to be less sensitive to ligand type than Ag and Cu, which could explain why certain Au TPNCs can be synthesized with different ligands. The low sensitivity of Au to the ligand type was explained through its larger IP compared to Ag and Cu. The metal IPs were used to connect the reaction free energies through a linear regression model. The model revealed a strong correlation between the break M-S and break S-R reactions across all metal-thiolate complexes, confirming the role of metal charge transfer on M-S-R bond strengths in these systems. Analogous bond breaking reactions were calculated on $[M_{25}(SR)_{18}]^-$ TPNCs by means of single ligand removal through two modes: R removal (break S-R) and SR removal (break M-S). The results showed the same trends in energetics as the M-S-R complex calculations. Once again, the break M-S reaction requires more energy due to the stronger M-S bond. Linear regression models were generated to investigate the relationship between M-S-R ligand removal energetics on molecular complexes and TPNC. Importantly, the results of the models showed that TPNC ligand removal energetics can be predicted solely from the respective molecular complex reaction energetics (ΔG^{bMS}, ΔG^{bSR}) and metal IPs. These results reveal that M-S-R bond energetics follow similar trends at both the molecular and nanoscale levels, introducing a new and rapid way to screen ligand removal energetics in TPNCs. Finally, computational mechanistic study on the hydrogenation pathways for SCH_3-based complexes revealed that, unlike Ag and Cu complexes, the Au complex prefers the break S-R over break M-S reaction, which follows the thermodynamic preference.

Supporting Information

Bar graphs of break M-S and break S-R reaction free energies for M-S-R complexes, calculated slopes of linear regression line (ΔG^{bMS} vs. ΔG^{bSR}) between M-S-R complexes with the same ligand, Mulliken charge distribution on M-S-R complexes for M = Ag, Au, Cu and SR = MBI, TG, Metal-Sulfur-Carbon (M-S-C) bond angle versus Metal-Nitrogen (M-N) distance for metal thiolate complexes for M = Ag, Au, Cu and SR = MBI, TG, M-H distances in TPNC break M-S products for A and B site reactions, parity plots of models to predict LRE^{bMS} from LRE^{bSR} and metal IP for A and B ligand removal sites, parity plots of models to predict TPNC LREs from A removal sites using ΔG^{bSR}, ΔG^{bMS}, and IP, mechanistic analysis of break M-S and break S-R energy barriers on $MSCH_3$.

Conflicts of Interest

There are no conflicts to declare.

References

1.   R. G. Nuzzo and D. L. Allara, *J. Am. Chem. Soc.*, 1983, **105**, 4481-4483.
2.   J. C. Love, L. A. Estroff, J. K. Kriebel, R. G. Nuzzo and G. M. Whitesides, *Chem. Rev.*, 2005, **105**, 1103-1170.

3.   P. E. Laibinis, G. M. Whitesides, D. L. Allara, Y. T. Tao, A. N. Parikh and R. G. Nuzzo, *J. Am. Chem. Soc.*, 1991, **113**, 7152-7167.

4.   A. Ulman, *Chem. Rev.*, 1996, **96**, 1533-1554.

5.   M. Brust, M. Walker, D. Bethell, D. J. Schiffrin and R. Whyman, *J. Chem. Soc., Chem. Commun.*, 1994, **0**, 801-802.

6.   R. Jin, H. Qian, Z. Wu, Y. Zhu, M. Zhu, A. Mohanty and N. Garg, *J. Phys. Chem. Lett.*, 2010, **1**, 2903-2910.

7.   P. D. Jadzinsky, G. Calero, C. J. Ackerson, D. A. Bushnell and R. D. Kornberg, *Science*, 2007, **318**, 430.

8.   M. J. Cowan and G. Mpourmpakis, *Dalton Trans.*, 2020, **49**, 9191-9202.

9.   R. Jin, C. Zeng, M. Zhou and Y. Chen, *Chem. Rev.*, 2016, **116**, 10346-10413.

10.   R. Jin, *Nanoscale*, 2015, **7**, 1549-1565.

11.   Y. Su, T. Xue, Y. Liu, J. Qi, R. Jin and Z. Lin, *Nano Res.*, 2019, **12**, 1251-1265.

12.   Z. Huang, F. Pu, Y. Lin, J. Ren and X. Qu, *Chem Commun (Camb)*, 2011, **47**, 3487-3489.

13.   J. Yang, F. Wang, H. Yuan, L. Zhang, Y. Jiang, X. Zhang, C. Liu, L. Chai, H. Li and M. Stenzel, *Nanoscale*, 2019, **11**, 17967-17980.

14.   Y. Tao, Y. Zhang, E. Ju, H. Ren and J. Ren, *Nanoscale*, 2015, **7**, 12419-12426.

15.   F. Muniz-Miranda, M. C. Menziani and A. Pedone, *Phys Chem Chem Phys*, 2014, **16**, 18749-18758.

16.   X. Cai, W. Hu, S. Xu, D. Yang, M. Chen, M. Shu, R. Si, W. Ding and Y. Zhu, *J. Am. Chem. Soc.*, 2020, DOI: 10.1021/jacs.9b07761.

17.   Y. Du, H. Sheng, D. Astruc and M. Zhu, *Chem. Rev.*, 2020, **120**, 526-622.

18.   T. Kawawaki, Y. Negishi and H. Kawasaki, *Nanoscale Adv.*, 2020, **2**, 17-36.

19.   Z. Y. Ma, P. Wang, L. Xiong and Y. Pei, *Wiley Interdiscip. Rev. Comput. Mol. Sci.*, 2017, **7**, e1315.

20.   P. Hu, L. Chen, X. Kang and S. Chen, *Acc Chem Res*, 2016, **49**, 2251-2260.

21.   R. Jin, *Nanoscale*, 2010, **2**, 343-362.

22.   H. Häkkinen, M. Walter and H. Grönbeck, *J. Phys. Chem. B*, 2006, **110**, 9927-9931.

23.   M. Rambukwella, N. A. Sakthivel, J. H. Delcamp, L. Sementa, A. Fortunelli and A. Dass, *Front. Chem.*, 2018, **6**, 330.

24.   S. Wang, X. Meng, A. Das, T. Li, Y. Song, T. Cao, X. Zhu, M. Zhu and R. Jin, *Angew. Chem. Int. Ed.*, 2014, **53**, 2376-2380.

25.   Y. Chen, C. Zeng, D. R. Kauffman and R. Jin, *Nano Lett.*, 2015, **15**, 3603-3609.

26.   H. Hakkinen, *Nat. Chem.*, 2012, **4**, 443-455.

27.   D. E. Jiang, *Nanoscale*, 2013, **5**, 7149-7160.

28.   D. M. Chevrier, L. Raich, C. Rovira, A. Das, Z. Luo, Q. Yao, A. Chatt, J. Xie, R. Jin, J. Akola and P. Zhang, *J Am Chem Soc*, 2018, **140**, 15430-15436.

29.   S. Hossain, Y. Imai, D. Suzuki, W. Choi, Z. Chen, T. Suzuki, M. Yoshioka, T. Kawawaki, D. Lee and Y. Negishi, *Nanoscale*, 2019, DOI: 10.1039/C9NR07117B.

30.   N. Austin, S. Zhao, J. R. McKone, R. Jin and G. Mpourmpakis, *Catal. Sci. Technol.*, 2018, **8**, 3795-3805.

31.   M. G. Taylor and G. Mpourmpakis, *Nat. Commun.*, 2017, **8**, 15988.

32.   A. V. Nagarajan, R. Juarez-Mosqueda, M. J. Cowan, R. Jin, D. R. Kauffman and G.

Mpourmpakis, *SN Appl. Sci.*, 2020, **2**, 680.

33. M. J. Frisch, G. W. Trucks, H. B. Schlegel, G. E. Scuseria, M. A. Robb, J. R. Cheeseman, G. Scalmani, V. Barone, G. A. Petersson, H. Nakatsuji, X. Li, M. Caricato, A. V. Marenich, J. Bloino, B. G. Janesko, R. Gomperts, B. Mennucci, H. P. Hratchian, J. V. Ortiz, A. F. Izmaylov, J. L. Sonnenberg, Williams, F. Ding, F. Lipparini, F. Egidi, J. Goings, B. Peng, A. Petrone, T. Henderson, D. Ranasinghe, V. G. Zakrzewski, J. Gao, N. Rega, G. Zheng, W. Liang, M. Hada, M. Ehara, K. Toyota, R. Fukuda, J. Hasegawa, M. Ishida, T. Nakajima, Y. Honda, O. Kitao, H. Nakai, T. Vreven, K. Throssell, J. A. Montgomery Jr., J. E. Peralta, F. Ogliaro, M. J. Bearpark, J. J. Heyd, E. N. Brothers, K. N. Kudin, V. N. Staroverov, T. A. Keith, R. Kobayashi, J. Normand, K. Raghavachari, A. P. Rendell, J. C. Burant, S. S. Iyengar, J. Tomasi, M. Cossi, J. M. Millam, M. Klene, C. Adamo, R. Cammi, J. W. Ochterski, R. L. Martin, K. Morokuma, O. Farkas, J. B. Foresman and D. J. Fox, *Journal*, 2016.

34. P. J. Stephens, F. J. Devlin, C. F. Chabalowski and M. J. Frisch, *The Journal of Physical Chemistry*, 1994, **98**, 11623-11627.

35. A. D. Becke, *The Journal of chemical physics*, 1993, **98**, 5648-5652.

36. L. E. Roy, P. J. Hay and R. L. Martin, *J Chem Theory Comput*, 2008, **4**, 1029-1031.

37. A. E. Reed and F. Weinhold, *J. Chem. Phys.*, 1983, **78**, 4066-4073.

38. J. P. Foster and F. Weinhold, *J. Am. Chem. Soc.*, 1980, **102**, 7211-7218.

39. K. B. Wiberg, *Tetrahedron*, 1968, **24**, 1083-1096.

40. J. VandeVondele, M. Krack, F. Mohamed, M. Parrinello, T. Chassaing and J. Hutter, *Comput. Phys. Commun.*, 2005, **167**, 103-128.

41. T. D. Kühne, M. Iannuzzi, M. Del Ben, V. V. Rybkin, P. Seewald, F. Stein, T. Laino, R. Z. Khaliullin, O. Schütt, F. Schiffmann, D. Golze, J. Wilhelm, S. Chulkov, M. H. Bani-Hashemian, V. Weber, U. Borštnik, M. Taillefumier, A. S. Jakobovits, A. Lazzaro, H. Pabst, T. Müller, R. Schade, M. Guidon, S. Andermatt, N. Holmberg, G. K. Schenter, A. Hehn, A. Bussy, F. Belleflamme, G. Tabacchi, A. Glöß, M. Lass, I. Bethune, C. J. Mundy, C. Plessl, M. Watkins, J. VandeVondele, M. Krack and J. Hutter, *J. Chem. Phys.*, 2020, **152**, 194103.

42. M. W. Heaven, A. Dass, P. S. White, K. M. Holt and R. W. Murray, *J. Am. Chem. Soc.*, 2008, **130**, 3754-3755.

43. M. D. Hanwell, D. E. Curtis, D. C. Lonie, T. Vandermeersch, E. Zurek and G. R. Hutchison, *J Cheminform*, 2012, **4**, 17.

44. J. P. Perdew, K. Burke and M. Ernzerhof, *Phys. Rev. Lett.*, 1996, **77**, 3865-3868.

45. J. VandeVondele and J. Hutter, *The Journal of Chemical Physics*, 2007, **127**, 114105.

46. S. Goedecker, M. Teter and J. Hutter, *Phys. Rev. B*, 1996, **54**, 1703-1710.

47. M. Walter, J. Akola, O. Lopez-Acevedo, P. D. Jadzinsky, G. Calero, C. J. Ackerson, R. L. Whetten, H. Gronbeck and H. Hakkinen, *Proc. Natl. Acad. Sci. U.S.A.*, 2008, **105**, 9157-9162.

48. X. Kang, H. Chong and M. Zhu, *Nanoscale*, 2018, **1**, 1758-1834.

49. S. Chen, S. Wang, J. Zhong, Y. Song, J. Zhang, H. Sheng, Y. Pei and M. Zhu, *Angewandte Chemie (International ed.)*, 2015, **54**, 3145-3149.

50. T. Higaki, Y. Li, S. Zhao, Q. Li, S. Li, X.-S. Du, S. Yang, J. Chai and R. Jin, *Angewandte Chemie (International ed.)*, 2019, **58**, 8291-8302.

51. N. A. Sakthivel and A. Dass, *Accounts of Chemical Research*, 2018, **51**, 1774-1783.

52. P. Chakraborty, A. Nag, A. Chakraborty and T. Pradeep, *Accounts of Chemical Research*, 2019,

52, 2-11.

53. Y. Zhu, H. Qian, M. Zhu and R. Jin, *Advanced materials (Weinheim)*, 2010, **22**, 1915-1920.

54. C. Sun, N. Mammen, S. Kaappa, P. Yuan, G. Deng, C. Zhao, J. Yan, S. Malola, K. Honkala, H. Häkkinen, B. K. Teo and N. Zheng, *ACS nano*, 2019, **13**, 5975-5986.

55. M. G. Taylor, N. Austin, C. E. Gounaris and G. Mpourmpakis, *ACS Catal.*, 2015, **5**, 6296-6301.

56. S. Li, D. Alfonso, A. V. Nagarajan, S. D. House, J. C. Yang, D. R. Kauffman, G. Mpourmpakis and R. Jin, *ACS Catal.*, 2020, **10**, 12011-12016.

57. Z. Wang, U. Wille and E. Juaristi, *Encyclopedia of physical organic chemistry*, John Wiley & Sons, Inc., Hoboken, New Jersey, 2017.

58. S. Malola and H. Häkkinen, *J. Am. Chem. Soc.*, 2019, **141**, 6006-6012.

59. Y. Kim and S. K. Kang, *Acta Crystallographica Section E*, 2015, **71**, 1058-1060.

60. Y.-N. Zhang, Y.-Y. Wang, L. Hou, P. Liu, J.-Q. Liu and Q.-Z. Shi, *CrystEngComm*, 2010, **12**, 3840-3851.

61. K. J. Heroux, K. S. Woodin, D. J. Tranchemontagne, P. C. B. Widger, E. Southwick, E. H. Wong, G. R. Weisman, S. A. Tomellini, T. J. Wadas, C. J. Anderson, S. Kassel, J. A. Golen and A. L. Rheingold, *Dalton Trans.*, 2007, **21**, 2150-2162.

62. D. R. Lide, *Handbook of Chemistry and Physics*, CRC Press, Boca Raton, FL, 73rd edn., 1992.

63. A. Dass, *Nanoscale*, 2012, **4**, 2260-2263.

64. M. Ma, L. Liu, H. Zhu, J. Lu and G. Tan, *Molecular Physics*, 2018, **116**, 1804-1811.

65. X. Kang, H. Chong and M. Zhu, *Nanoscale*, 2018, **10**, 10758-10834.

66. J. Akola, M. Walter, R. L. Whetten, H. Hakkinen and H. Gronbeck, *J. Am. Chem. Soc.*, 2008, **130**, 3756-3757.

67. Z. Wu and R. Jin, *ACS Nano*, 2009, **3**, 2036-2042.

68. G. Salassa, A. Sels, F. Mancin and T. Burgi, *ACS Nano*, 2017, **11**, 12609-12614.